Structural Studies of the Neural-Cell-Adhesion Molecule by X-ray and Neutron Reflectivity†

Colin P. Johnson,‡ Giovanna Fragneto,§ Oleg Konovalov,|| Virginie Dubosclard,⊥ Jean-Francois Legrand,⊥ and Deborah E. Leckband*,‡,#,¶

Department of Chemistry, University of Illinois at Urbana-Champaign, Urbana, Illinois 61801, Institute Laue Langevin, BP 156, 38042, Grenoble Cedex, France, European Synchrotron Radiation Facility, BP 220, 38043 Grenoble Cedex, France, UMR 5819 (CEA-CNRS-Universite J. Fourier), 17 Av. des Martyrs 38054 Grenoble Cedex 9, France, and Department of Chemical and Biomolecular Engineering and Center for Biophysics and Computational Biology, University of Illinois at Urbana-Champaign, Urbana, Illinois 61801

Received August 12, 2004; Revised Manuscript Received October 28, 2004

ABSTRACT: The structures of adhesion proteins play an important role in the formation of intercellular junctions and the control of intermembrane spacing. This paper describes the combination of neutron and X-ray specular reflectivity measurements to investigate the structure of the ectodomain of the neural-cell-adhesion molecule (NCAM). The measurements with unmodified NCAM suggest the presence of a bend in the extraceullar region. Measurements with the polysialic-acid-modified form of NCAM reveal that, at physiological ionic strength, the carbohydrate chains extend beyond the range of the unmodified protein. The excluded volume of the polymer is also ionic-strength-dependent, as expected for a polyelectrolyte. The structural characteristics obtained from these independent analyses of X-ray and neutron reflectivity data agree with each other, with prior reflectivity studies, and with molecular dimensions obtained from direct-force measurements. These results provide structural insights into the configuration of the NCAM ectodomain and the regulation of NCAM adhesion by post-translational modification.

The neural-cell-adhesion molecule (NCAM)[1] is expressed in both developing and adult vertebrate organisms and is a cell-surface glycoprotein, which mediates cell adhesion, signaling, migration, and plasticity in the central nervous system (*1*). NCAM binds homophilically to other NCAM molecules on opposing cell surfaces. *In vivo* studies with mice showed that the inhibition of NCAM function by anti-NCAM antibodies prevents long-term memory formation (*2*). Several isoforms of NCAM are expressed, with the three most prominent differing in their membrane attachment (*3*). Despite these differences, all isoforms possess an extracellular region composed of five tandem immunoglobulin (Ig) domains followed by two membrane-proximal fibronectin type-III (FNIII) domains (*4*). Electron microscopy studies of the extracellular region exhibited a range of NCAM conformations that appeared to result from a flexible bend between the Ig domains and the FNIII domains (*5*, *6*). The authors concluded that NCAM does not extend perpendicular to the membrane but is instead bent at a flexible hinge between the two regions of the protein.

One of the more interesting properties of NCAM is that it is found in two forms, namely, an adhesive form and an antiadhesive form. In the early stages of development, NCAM is post-translationally modified with up to two linear α,2,8-polysialic acid (PSA) chains N-linked at distinct sites on the fifth Ig domain (*7*). In contrast to the unmodified protein, the PSA−NCAM exhibits antiadhesive properties (*8*, *9*). The post-translational modification of NCAM enhances cell motility, increases intercellular space, and increases neural plasticity (*8*, *10*−*12*). The lengths of the carbohydrate chains vary widely, with the degree of polymerization exceeding 55 monomers (*13*). The sialic acid monomers are negatively charged, and intersegment repulsion increases the excluded volume of the chains (*14*). Adhesion between PSA−NCAM expressing cells also depends on the ionic strength (*15*). At physiological ionic strength, the cells did not adhere, but adhesion recovered at high (0.5 M) salt concentrations. This was attributed to the reduction in the excluded volume of PSA because of electrostatic screening, which in turn reduced the intercellular repulsion and

† Funding was provided by the UIUC-CNRS cooperation program and by the National Institutes of Health RO1 GM33986.

* To whom correspondence should be addressed: Department Chemical and Biomolecular Engineering, 127 Rodger Adams Laboratory, 600 S. Mathews Ave., Urbana, IL 61801. Telephone: 217-244-0793. Fax: 217-333-5052. E-mail: leckband@uiuc.edu.

‡ Department of Chemistry, University of Illinois at Urbana-Champaign.

§ Institute Laue Langevin.

|| European Synchrotron Radiation Facility.

⊥ UMR 5819 (CEA-CNRS-Universite J. Fourier).

Department of Chemical and Biomolecular Engineering, University of Illinois at Urbana-Champaign.

¶ Center for Biophysics and Computational Biology, University of Illinois at Urbana-Champaign.

[1] Abbreviations: SLD, scattering length density; XR, X-ray reflectivity; NR, neutron reflectivity; CAM, cell-adhesion molecule; NCAM, neural-cell-adhesion molecule; PSA, polysialic acid; FNIII, fibronectin type-III domain; Ig, immunoglobulin; HEPES, 4-(2-hydroxyethyl)-1-piperazineethanesulfonic acid; DPPE, dipalmitoyl phosphatidyl ethanolamine; DPPC, 1,2-dipalmitoyl-*sn*-glycero-3-phosphocholine; NTA-TRIG-DLGE, 6-(9-(2,3-bis(dodecyloxy)propyl)-3,6,9-trioxanonyl-1-oxycarboxylamino)-2-(di(carboxylmethyl)amino)hexanoic acid; DTPC, ditridecanoyl phosphatidyl choline; LB, Langmuir−Blodgett.

10.1021/bi048263j CCC: $30.25
Published on Web 00/00/0000 PAGE EST: 9

increased the adhesion. However, there is no study that directly demonstrated the molecular basis of this behavior or quantified the dimensions of the carbohydrate under these different conditions.

PSA may inhibit cell adhesion by sterically impeding the close approach and adhesion between adjacent cells (*9*, *11*, *12*, *16*). This so-called trans-inhibition mechanism would require the chains to extend at least to the outermost adhesive domains of NCAM, so that the resulting osmotic repulsion would offset the specific attraction at the same membrane separation. On the other hand, the PSA could disrupt the lateral (cis) clustering of adhesion molecules and thereby prevent the formation of adhesive junctions. Here, the lateral extension of the chains would only need to block interactions between adjacent proteins (*1*). Quantitative measurements of the polymer extension relative to the protein dimensions would therefore provide important structural insights into the underlying mechanism by which the PSA modification regulates NCAM function.

In this study, both X-ray reflectivity (XR) and neutron reflectivity (NR) measurements determined the extension of the membrane-bound NCAM ectodomain and of PSA−NCAM monolayers supported on lipid membranes. The two techniques are very complementary because a better contrast between the different layers is obtained with the neutrons, while a higher spatial resolution is reached with the X-rays. They reveal details at the angstrom level of this well-characterized system. Here, NCAM and PSA−NCAM were engineered with C-terminal polyhistidine tails. These proteins were in turn immobilized and oriented on nitrilotriacetic acid (NTA)-modified lipid monolayers. From the electron-density and neutron scattering-length-density (SLD) profiles perpendicular to the lipid surface, we determined the dimensions of the proteins and associated PSA. These results indicate that there is a bend in the full ectodomain structure, in agreement with previous electron microscopy studies (*5*, *6*). Studies with PSA−NCAM at physiological NaCl concentrations indicate that the carbohydrate chains extend beyond the protein. In 1 M NaCl, both the electron density and the SLD increase near the glycoprotein base, at the expense of the density at larger distances. The latter is indicative of the collapse of the carbohydrate chains at high ionic strength because of electrostatic screening.

MATERIALS AND METHODS

Materials. The synthetic lipids 1,2-dipalmitoyl-*sn*-glycero-3-phosphoethanolamine (DPPE) and 1,2-dipalmitoyl-*sn*-glycero-3-phosphocholine (DPPC) were from Avanti Polar Lipids. Hydrogenated 6-[9-[2,3-bis(dodecyloxy)propyl]-3,6,9-trioxanonyl-1-oxycarboxylamino]-2-[di(carboxymethyl)amino]hexanoic acid (NTA-TRIG-DLGE) was custom synthesized by Northern Lipids, Inc. (Vancouver, BC, Canada). 1-Octadecanethiol, 4-(2-hydroxyethyl-1-piperazineethanesulfonic acid (HEPES), sodium chloride, and nickel sulfate were from Aldrich. Silicon blocks used for the neutron experiments were purchased from Siltronix (Archamps, France).

Protein Expression and Purification. The proteins were isolated from the cell-culture supernatants of stably transfected Chinese hamster ovary (CHO) cells, as described previously (*17*). The purification of the secreted polyhistidine-tagged proteins involved a three-step process, in which the cell medium was first passed over a Ni-NTA affinity column (Qiagen), and the protein was eluted with a buffer containing 200 mM imidazole. The resulting protein eluant was then purified by anion-exchange chromatography and finally purified to homogeneity with a gel-filtration column. Cell transfection and selection, as well as the protein expression protocols, were described previously (*17*).

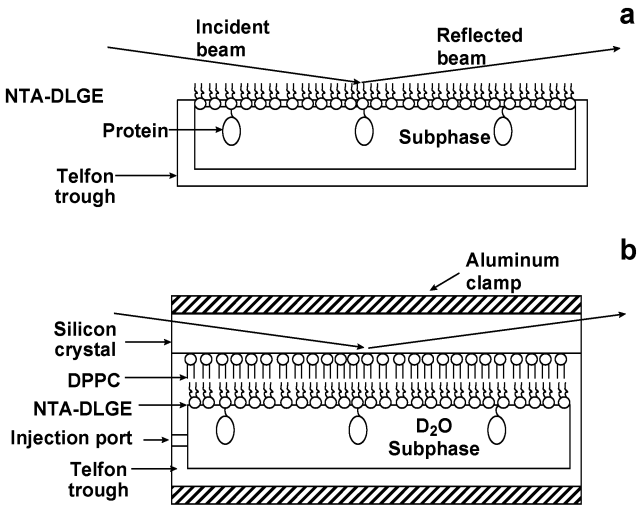

FIGURE 1: (a) Schematic of the lipid monolayer and trough used in XR measurements. (b) Schematic of the supported lipid bilayer and sample holder for NR studies. The protein is immobilized to the lipid bilayer, which is supported on an oxidized silicon block. The silicon proximal lipid layer is gel-phase DPPC, and the distal lipid film is fluid NTA-TRIG-DLGE.

Specular XR Setup. XR measurements were conducted at beamline ID10B at the European Synchrotron Radiation Facility (ESRF) in Grenoble, France. The instrumental setup has been described elsewhere (*18*, *19*). Briefly, the vertical aperture was set to 0.1 mm, and the horizontal aperture was set to 1 mm. The selected wavelength was 0.154 nm at the critical angle formed between the beam and aqueous subphase ($\theta_c = 0.1525°$ at the energy used). The footprint of the X-ray beam was half the length of the trough. For the sample preparation, a stock solution of NTA-TRIG-DLGE dissolved in chloroform at a concentration of 1 mg/mL was spread at the air−water interface of the 15 mL Teflon trough. The trough had been precleaned with Piranha solution comprising HCl, H_2O_2, and H_2O in a 1:1:1 ratio by volume. The surface area of the trough was 80×60 mm^2, and the surface pressure of the lipid monolayer was monitored with a Wilhelmy balance (NIMA). The aqueous subphase contained 20 mM HEPES, 100 mM NaCl, and 15 μM $NiSO_4$ at pH 7.7, and drops of NTA-TRIG-DLGE solution were spead until a surface pressure of approximately 36 mN/m was obtained. Protein adsorption to the NTA-TRIG-DLGE headgroup proceeded following the protein injection into the subphase to achieve micromolar concentrations. Figure 1a shows the resulting monolayer and sample configuration. Reflectivity measurements were conducted after incubation with the protein for at least 1 h at room temperature. During the measurements, the sample was enclosed in a helium-filled chamber to reduce oxidation and to minimize the parasitic background because of small-angle scattering of the X-ray beam by air. Measurements were made up to a momentum transfer of $Q_z = 5$ nm^{-1}, using a position-

sensitive detector (PSD) aligned parallel to the plane of incidence and perpendicular to the water surface. The trough sample was slowly translated perpendicular to the X-ray beam during the measurement, to minimize beam exposure and to thereby avoid radiation damage to the sample by the beam. All X-ray measurements were taken at room temperature. To account for evaporation of the subphase and possible lowering of the sample surface, a water level controller (Nanofilm GmBH, Germany) regulated the height of the subphase. The data were analyzed with the reflectivity analysis program Parratt32 version 1.5.2 (Hahn Meitner Institute, Berlin, Germany). The χ^2 values for the fits were determined from the weighted fits to the data. The error in the data defined the statistical weight of each data point. The range of parameter values that fell within 10% of the globally minimized fit then determined the error in the fitted parameters.

To change the subphase composition, the trough was connected via an inlet port to a reservoir via a peristaltic pump. Flushing at least 3 trough volumes (45 mL) of buffer through the trough via inlet and outlet ports exchanged the subphase buffer. For buffer exchanges, the outlet port was directed to waste.

Specular NR Setup. NR experiments were performed on the D17 reflectometer at the Institut Laue Langevin in Grenoble, France (*20*). Measurements were made in time-of-flight mode with a spread of wavelength from 0.2 to 2 nm, and the full Q range was attained by overlapping the measurements obtained at two values of the incoming beam angle, that is, at 0.7° and 3°. For the measurements of the second part of the reflectivity profile, the resolution was relaxed. In addition, short 1 h scans at the first angle (=0.7°) were also conducted, to confirm that protein adsorption to the membrane occurred after protein injection into the subphase.

The sample substrate was a polished $5 \times 5 \times 1$ cm^3 single-crystal, silicon block with atomic surface roughness (Siltronix, Archamps, France). The surface of the block was first cleaned with chloroform and ethanol and then oxidized by exposure to UV radiation under a flow of pure oxygen. After oxidation, a lipid bilayer was deposited on the silicon block. The first lipid layer was a pure, gel-phase DPPC monolayer formed by Langmuir−Blodgett (LB) deposition onto the silicon at a constant pressure of 40 mN/m. A second, outer lipid layer of fluid Ni-NTA-TRIG-DLGE was then transferred by Langmuir−Schaefer deposition, at a constant surface pressure of 36 mN/m. After bilayer deposition, the substrate was placed on a Teflon trough 0.3 mm deep, with a small volume of buffered subphase between the trough and bilayer sample (Figure 1b). The assembly was then clamped together with bolted aluminum plates (Figure 1b) as described previously (*21*). The injection of protein solution into the subphase to micromolar concentrations initiated protein immobilization to the bilayer. The protein adsorption proceeded for at least 1 h before measurements were taken at room temperature. To change the solvent contrast or ionic strength, the same sample was flushed with at least four trough volumes of the new buffer, while directing the excess solution to waste. Thus, the properties of the same sample were measured under different solution conditions.

Surface Plasmon Resonance. Surface plasmon resonance measurements were conducted with a home-built plasmon resonance instrument in the Kretchman configuration, described previously (*22*). The sample substrate consisted of a monolayer of 100% NTA-TRIG-DLGE deposited onto a self-assembled hexadecanethiol monolayer on gold films. The thin gold films (36 nm) were thermally evaporated on glass slides, which were first coated with a 1 nm chromium adhesion layer. The supported lipid monolayer was mounted in a flow cell.

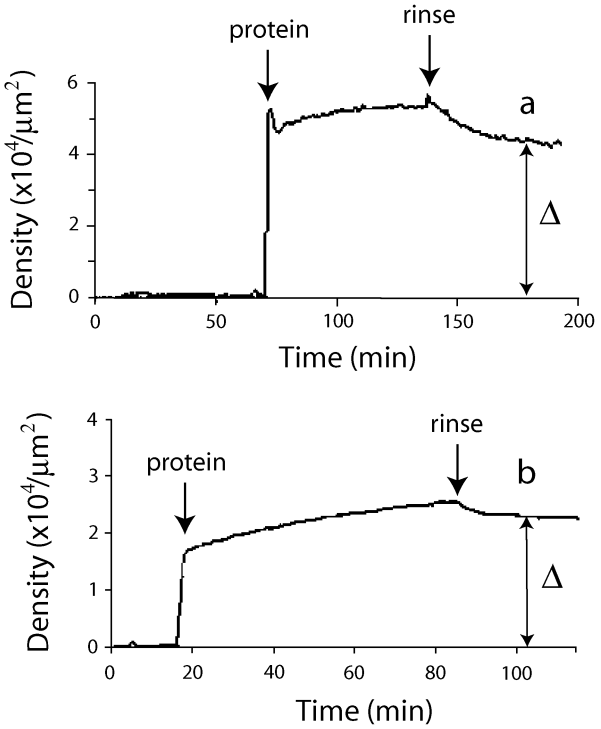

FIGURE 2: PSA−NCAM-His$_{10}$ (a) and NCAM-His$_{10}$ (b) adsorption time courses measured by surface plasmon resonance. Upon injection of the protein solution, there is a sharp increase in the effective optical thickness of the adlayer (arrow). After a rinse with pure buffer, the difference between the initial and final signal, Δ, indicated by the vertical arrows, gives the total amount of immobilized protein bound to the surface.

Protein adsorption to the supported NTA−lipid monolayers was determined after first recording a baseline signal with a solution containing 20 mM HEPES, 100 mM NaCl, and 10 μM $NiSO_4$ at pH 7.7 (Figure 2). The subsequent injection of protein and its adsorption to the lipid layer generated a shift in the plasmon resonance angle. The total adsorbed amount Δ was quantified by fitting the change in the resonance angle with the Fresnel reflectivity equations (*22*, *23*). The refractive index of a densely packed protein layer was assumed to be 1.44 (*24*). The surface was then washed to remove nonspecifically adsorbed protein. The difference between the initial and final resonance angles was used to determine the total amount of bound protein.

RESULTS

Surface Plasmon Resonance. Parts a and b of Figure 2 show the adsorption time courses obtained with PSA−NCAM-His$_{10}$ and NCAM-His$_{10}$, respectively. We first recorded a baseline signal with pure buffer. After the injection of the polyhistidine-tagged proteins, there was a significant shift in the plasmon resonance angle (Figure 2). After rinsing with buffer, the total difference between the final and initial signals (Δ in Figure 2) gave the amount of protein adsorbed.

On a 100% NTA-TRIG-DLGE monolayer, the surface density of NCAM-His_{10} was $2.3 \pm 0.9 \times 10^4/\mu m^2$, while the PSA−NCAM-$His_{10}$ coverage was $4.3 \pm 0.9 \times 10^4/\mu m^2$. Including 10 mM ethylenediaminetetraacetic acid (EDTA) in the running buffer confirmed the adsorption specificity of both NCAM and PSA−NCAM. EDTA chelates nickel ions and prevents binding between the NTA headgroups and histidine. Measurements with EDTA in the buffer showed no appreciable adsorption of either NCAM-His_{10} or PSA−NCAM-His_{10}. The difference in surface density indicates that PSA−NCAM packs more densely than NCAM when bound to the lipid monolayer. This difference is further supported by the NR results described below.

XR: Lipid Monolayer. XR profiles were first generated with a pure Ni-NTA-TRIG-DLGE monolayer at the air−water interface of the Teflon trough, before adding the protein. Figure 3a shows the reflectivity profile for the NTA-TRIG-DLGE monolayer, which was also described previously (*25*). We analyzed the reflectivity profile for the lipid monolayer with the fitting program Parratt32 (Hahn Meitner Institute, Berlin, Germany), which fits the data using a series of box layers, each with a distinct electron density, thickness, and roughness factor. The parameters of the box model were continuously adjusted to obtain the best model fit to the experimental data, as defined by minimizing χ^2. The reflectivity curve in Figure 3a is best described with a two-layer box model (—, Figure 3a). The thickness of the first layer is 12.2 ± 1 Å with an electron density of 0.24 ± 0.04 $e^-/Å^3$ and corresponds to the alkane region of the lipid (Table 1). This closely matches the 14.5 Å thickness determined previously (*25*). Likewise, the second 17.3 ± 1 Å layer corresponds to the lipid headgroup and spacer. This gives a total thickness of 29.4 Å, in quantitative agreement with the previous findings (*25*).

NCAM. Figure 3a also shows the XR profile obtained with the full NCAM ectodomain, NCAM-His_{10}, bound to the NTA-TRIG-DLGE monolayer. This is plotted with the profile of the lipid layer for comparison. The clear shifts in the curve show that NCAM binds to the lipid monolayer. In addition, fits of the spectrum to the two-layer lipid monolayer model resulted in a poor fit ($\chi^2 = 7.03$). However, the addition of a single-box layer to the lipid model described the reflectivity profile (Figure 3a). The electron density of the solvent was also adjusted for the added salt. The fitted values for the lipid layer changed little, despite being allowed to vary in the fitting process. The NCAM layer thickness might be expected to be approximately 280 Å (=7 × 40 Å) because of the seven domains, if the protein lacked a hinge and aligned perpendicular to the membrane. However, the data analysis gives the best fit with an additional 206 ± 7 Å protein layer with a 9.6 ± 3 Å roughness factor (Figure 3a and Table 1). Although this is shorter than the 280 Å end−end length of the extended protein, it is not unexpected. Force measurements between opposed NCAM-His_{10} monolayers on supported bilayers also indicated a smaller steric thickness than expected for a fully extended protein (*17*).

Figure 3c shows the electron-density profile of the supported NCAM monolayer. The fitted electron density for the protein box is 0.35 ± 0.02 $e^-/Å^2$. The electron density of a protein is 0.42 $e^-/Å^2$ (*26*), and the electron density of the solvent containing 100 mM NaCl is 0.335. On the basis of the NCAM surface density on a NTA-TRIG-DLGE monolayer (2.5×10^{-17} m^2/NCAM), measured by SPR and isotope labeling (*17*), and on the crystallographic dimensions of one of the seven NCAM domains (radius of 11 Å, and height of 40 Å), the estimated volume fraction of NCAM in the protein layer is ~0.20. The calculated average electron density of the hydrated protein layer is therefore ~0.35 $e^-/Å^2$

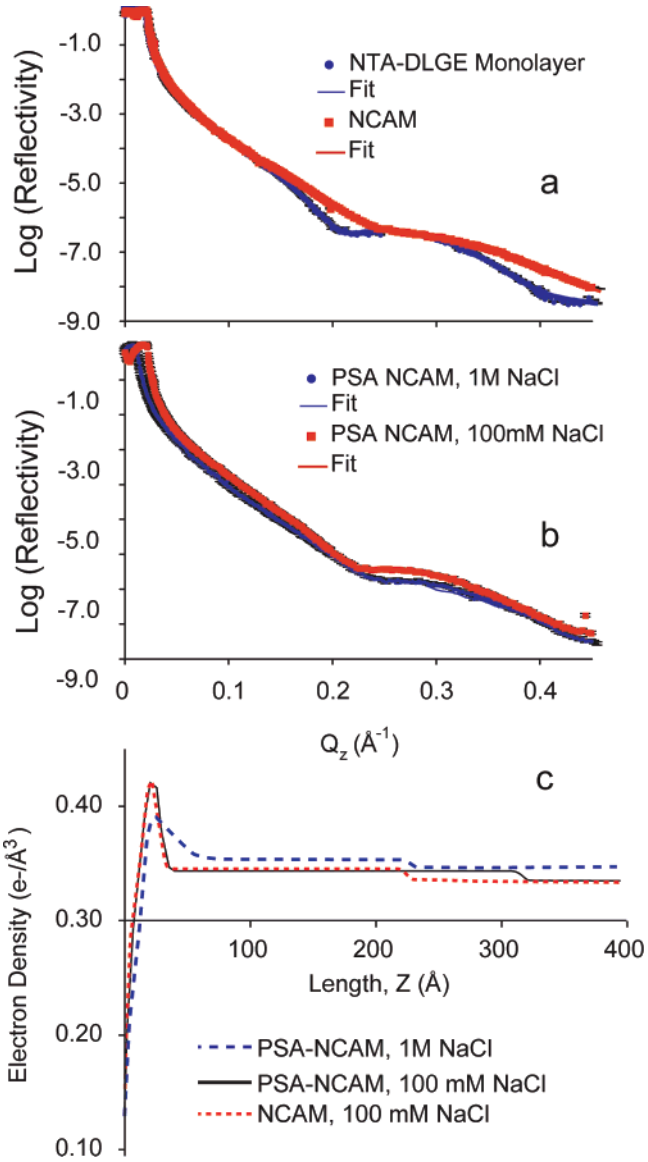

FIGURE 3: Specular XR profiles of NCAM and lipid monolayers. (a) Reflectivity profiles of the NTA-DLGE monolayer (blue circles) and immobilized NCAM-His_{10} (red squares) immobilized on an NTA-TRIG-DLGE monolayer at the air−water interface. The error bars are the size of the data points. The subphase in both cases contained 100 mM NaCl. The solid lines follow the data within error and are the best model fits to the data. (b) Specular XR profiles of immobilized PSA−NCAM-His_{10} immobilized on an NTA-TRIG-DLGE monolayer at the air−water interface in 1 M NaCl (blue circles) and 100 mM NaCl (red squares). The sizes of the symbols are the same as the error bars. The solid lines, which follow the data within the limits of error, are the best model fits to the data. The model parameters are in Table 1. (c) Calculated electron-density profiles of NCAM and PSA−NCAM monolayers. Here, $Z = 0$ corresponds to the ends of the alkane tails. The solid line is the electron-density profile for the unmodified NCAM convolved with a Gaussian smoothing function to account for the roughness. The red dotted line shows the model profile for NCAM in 100 mM NaCl; the black solid line shows the model profile for PSA−NCAM in 100 mM NaCl; and the blue dashed line shows the profile for PSA−NCAM in 1 M NaCl.

Table 1: Model Parameters Obtained from Fits of XR Profiles

sample (layers)	thickness (Å)	density ($e^-/Å^3$)	roughness (Å)	χ^2
lipid				
1 alkane	12.2 ± 1	0.24 ± 0.01	4 ± 1	
2 headgroup	17.3 ± 1	0.52 ± 0.07	4 ± 2	
3 solvent		0.335	4 ± 2	0.18
NCAM				
1 alkane	13.5 ± 1	0.3 ± 0.04	4 ± 1	
2 headgroup	16 ± 1	0.48 ± 0.07	4 ± 1	
3 protein	206 ± 7	0.35 ± 0.02	5 ± 2	
4 solvent		0.335	9.6 ± 3	0.70
PSA−NCAM (100 mM NaCl)				
1 alkane	13 ± 1	0.28 ± 0.04	4 ± 2	
2 headgroup	15 ± 1	0.46 ± 0.03	4 ± 1	
3 protein	290.9 ± 5	0.35 ± 0.01	8.8 ± 2	
4 solvent		0.335	15 ± 4	0.23
PSA−NCAM (1 M NaCl)				
1 alkane	13.7 ± 1	0.24 ± 0.08	4 ± 1	
2 headgroup	19.2 ± 2	0.43 ± 0.02	4.2 ± 1	
3 protein	190 ± 7	0.36 ± 0.01	8 ± 1	
4 solvent		0.346	25 ± 5	0.29

[=(0.2 × 0.42) + (0.8 × 0.335)], in good agreement with the fitted value.

PSA-Modified NCAM (PSA−NCAM). To determine the segment density profile of the carbohydrate chains relative to both the membrane and the NCAM ectodomain, PSA−NCAM-His_{10} was bound to the Ni-NTA-TRIG-DLGE monolayer, as described for NCAM-His_{10}. Figure 3b (blue circles) shows the reflectivity profile of the PSA−NCAM-His_{10} in a buffer containing 100 mM NaCl. These data were best-fit by adding a third layer to the two-layer lipid model. The fitted glycoprotein layer thickness was 291 ± 10 Å with an electron density of 0.35 ± 0.01 (Table 1). Again, the values for the alkane layer and lipid headgroup of the NTA-TRIG-DLGE did not change significantly upon protein binding (Table 1). The calculated electron-density profile is shown in Figure 3c. The 291 Å thickness exceeds that of the NCAM-His_{10} monolayer, although the low contrast between the carbohydrate and water prevents determining the exact thickness of the glycoprotein.

The model fit also exhibits a large degree of roughness (15 ± 4 Å) between the glycoprotein and the bulk solvent (Table 1). Because the electrostatic repulsion between sialic residues increases the carbohydrate (polyelectrolyte) swelling, the large polymer extension and increased thickness of the glycoprotein layer is expected. The diffuse polymer−solvent interface and the polydispersity of PSA can account for the roughness.

Previous studies suggested that the charges of the sialic acid monomers contribute substantially to the repulsive properties of the carbohydrate (*15*, *27*). The electrostatic repulsion between segments swells the polyelectrolyte. The charges are screened at high ionic strength, so that the radius of gyration and hence the excluded volume decrease with increasing salt concentration (*14*, *27*). To quantify the effect of the ionic strength on the PSA extension, we repeated the measurements of PSA−NCAM-His_{10} with 1 M NaCl in the buffered subphase. To do this, we used the same protein monolayer but exchanged the subphase. This ensured that changes in the profile were solely due to the influence of the ionic strength on the carbohydrate configuration.

Figure 3b shows the XR profile for PSA−NCAM in 1 M NaCl (red squares). In this case, the reflectivity spectrum was also fit by adding an additional box with a thickness of 190 ± 7 Å to the lipid model (Table 1). Again, the electron density of the solvent was adjusted for the added salt. In comparison to the XR data obtained with 100 mM NaCl, the best-fit model clearly shows a large shift in the electron-density profile (Table 1). The glycoprotein thickness is much smaller than that of the PSA−NCAM in 100 mM NaCl. The electron density was also slightly higher at 0.361 ± 0.01 $e^-/Å^3$. Figure 3c shows the calculated electron-density profile. This reduction in the overall thickness and concomitant increase in the electron density near the membrane indicate that the PSA chains collapse at the higher salt concentration. Concomitant with the changes in the glycoprotein parameters, we also note that the fitted electron density of the lipid headgroup decreases slightly. This may be due to the increased PSA-segment density near the lipid headgroup. This could reduce the contrast between the two layers, so that the fitted electron-density parameter would be closer to an average of the two boxes.

NR: Lipid Bilayer. NR studies were also conducted with NCAM-His_{10} and PSA−NCAM-His_{10} immobilized on lipid bilayers supported on silicon blocks (Figure 1b). Reflectivity measurements were first conducted with the bare silicon block to determine the thickness of the superficial oxide layer and to quantify the surface roughness. Then, all of the measurements were performed with two buffer solutions of different SLD, namely, D_2O solutions with a SLD of 6.4 × 10^{-6} $Å^{-2}$ and "silicon-matched water" (SMW) and a blend of H_2O/D_2O with a SLD of 2.1 × 10^{-6} $Å^{-2}$. The parameters were determined by globally fitting the data obtained with both solvent contrasts, using AFIT (*28*). This program fits the NR spectra to a series of box layers with parameters for each box that are each allowed to vary. Parameters used for model fitting include the thickness, SLD, roughness, and degree of hydration. The measured SLD β_{meas} is

$$\beta_{meas} = x\beta_{layer} + (1 - x)\beta_{solvent} \quad (1)$$

where x is the volume fraction of the adlayer and β_{layer} and $\beta_{solvent}$ are the SLDs of the layer, e.g., protein or hydrocarbon and solvent, respectively.

The parameters for the single-box layer used to describe the silicon block were varied independently until a best fit between the theoretical model and experimental spectrum was obtained. Fitting the NR data measured with the bare silicon gave a 12 ± 2 Å oxide layer, with a 3 ± 2 Å roughness and an SLD of 3.4 ± 0.1 × 10^{-6} $Å^{-2}$. This agrees with previously determined values for UV/ozone-treated silicon-block surfaces (*29*).

After the characterization of the oxide layer, a lipid bilayer composed of a gel-phase DPPC inner leaflet and a fluid Ni-NTA-TRIG-DLGE outer leaflet was deposited on the silicon block (Figure 1b). The NR profile was then measured in both buffered D_2O (Figure 4a) and SMW. The constraints imposed by the simultaneous (global) fitting of both solvent contrasts yielded a unique model, composed of five layers (Figure 4a and Table 2). The use of fewer boxes gave poorer fits. The first layer after the silicon oxide is a 5 ± 2 Å water film. Adjacent to this is the 6 ± 2 Å DPPC headgroup, with an SLD of 1.3 ± 0.3 × 10^{-6} $Å^{-2}$, followed by a 32 ± 1 Å

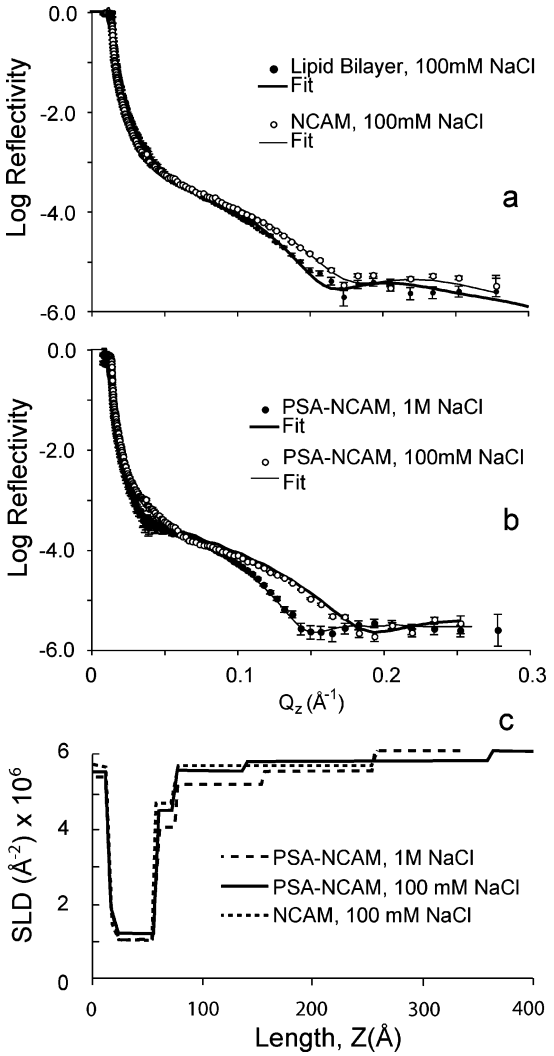

FIGURE 4: Specular NR profiles of NCAM and lipid monolayers. (a) NR profile of the silicon-supported lipid bilayer (●) and immobilized NCAM-His_{10} (○) monolayers on the silicon-supported lipid bilayer. The solid lines are the best model fits to the data. (b) Specular NR profile of PSA−NCAM-His_{10} immobilized on a supported lipid bilayer in 1 M NaCl (●) and 100 mM NaCl (○). The solid lines are the best model fits to the data. (c) SLD profiles of NCAM and PSA−NCAM on a lipid bilayer supported on the silicon block. Here, $Z = 0$ is the silicon−silicon oxide interface. The dotted line shows the model profile for NCAM in 100 mM NaCl; the solid line shows the model profile for PSA−NCAM in 100 mM NaCl; and the dashed line shows the profile for PSA−NCAM in 1 M NaCl.

alkane layer and a 19 ± 3 Å layer for the hydrated headgroup and NTA linker (Table 2). Figure 4c shows the calculated SLD profile. In the region corresponding to the lipid alkane chains, the SLD is higher than expected at 0.74 ± 0.1 × 10^{-6} Å^{-2}. Nevertheless, the fits were highly sensitive to the SLD of this layer, with deviations of ±0.01 worsening the fit significantly. Moreover, this higher-than-expected value was consistent across all of the samples investigated. Even though the XR and NR curves were obtained with different samples and fit independently, the best-fit model parameters for the NTA-TRIG-DLGE monolayer agree closely with those obtained from the XR data.

NCAM. To determine the thickness of the immobilized NCAM-His_{10} bound to the lipid bilayer, we carried out NR measurements of the protein monolayer with both D_2O and SMW contrasts. The NCAM was assembled onto the same bilayer used to generate the bilayer data. The NCAM-His_{10} reflectivity spectrum is also shown in Figure 4a, for comparison. There are statistically significant changes in the spectrum upon protein binding, at both low and high Q_z. The best model fit to the data (Figure 4a), obtained with both the hydrated D_2O and SMW buffers, is a six-box model in which the protein is described by a single additional layer and the NTA headgroup and linker are described by a single layer. Values for each parameter in the model could vary during the fits. This included the parameters for the lipid bilayer, to account for any changes induced by protein adsorption. Table 2 summarizes the best-fit model parameters. The NTA headgroup and linker have nearly the identical overall thickness of 19 ± 3 Å (Table 2) compared with the X-ray results. The roughness of the lipid headgroup box increased slightly to 9 ± 3 Å. This difference is subtle, but it may be due to some disordering of the headgroup upon protein adsorption. Figure 4c shows the corresponding SLD profile. The fact that the values for the other lipid layers were virtually unchanged indicates no membrane disruption. The fitted thickness of NCAM-His_{10} was 199 ± 5 Å, with a SLD of 3.0 ± 0.3 × 10^{-6} Å^{-2} and a roughness of 12 ± 4 Å (Table 2). This agrees qualitatively with the XR results.

PSA−NCAM. The steric dimensions of PSA−NCAM-His_{10} were also investigated at low (100 mM) and high (1 M) NaCl concentrations. Figure 4b shows the NR profile obtained with immobilized PSA−NCAM-His_{10} in a buffered D_2O subphase containing 100 mM NaCl. In this case, the addition of two additional boxes to the lipid model gave the best fit to the data. The separation of the outer PSA−NCAM-His_{10} into two layers increased the sensitivity of the fits to gradients in the SLD (*30*). Table 2 summarizes the best-fit

Table 2: Fitted Parameters from the Models of the NR Profiles

sample (layers)	thickness (Å)	SLD (×10^{-6} Å^{-2})	hydration (%)	roughness (Å)	χ^2
lipid					
1 silicon	12 ± 2	3.4 ± 0.1	0 ± 3	3 ± 2	
2 water	5 ± 2		100	2 ± 1	
3 headgroup	6 ± 2	1.3 ± 0.3	3 ± 2	4 ± 2	
4 alkane	32 ± 1	0.7 ± 0.1	6 ± 3	4 ± 2	
5 headgroup	19 ± 3	2.7 ± 0.2	52 ± 5	6 ± 3	1.4
NCAM					
1 silicon	10 ± 3	3.4 ± 0.1	0 ± 3	4 ± 2	
2 water	5 ± 2		100	1 ± 1	
3 headgroup	6 ± 2	1.3 ± 0.3	5 ± 2	1 ± 1	
4 alkane	32 ± 1	0.7 ± 0.1	4 ± 2	4 ± 2	
5 headgroup	19 ± 3	2.5 ± 0.2	45 ± 5	9 ± 3	
6 protein	199 ± 5	3.0 ± 0.3	87 ± 4	12 ± 4	2.1
PSA−NCAM (100 mM NaCl)					
1 silicon	10 ± 3	3.4 ± 0.1	0 ± 3	3 ± 2	
2 water	5 ± 2		100	2 ± 1	
3 headgroup	5 ± 2	1.2 ± 0.3	10 ± 3	2 ± 2	
4 alkane	32 ± 1	0.7 ± 0.1	7 ± 3	4 ± 2	
5 headgroup	24 ± 5	2.0 ± 0.4	46 ± 4	12 ± 3	
6 protein	115 ± 5	3.6 ± 0.4	74 ± 4	12 ± 4	
7 protein	162 ± 6	4.2 ± 0.4	83 ± 5	12 ± 4	2.3
PSA−NCAM (1 M NaCl)					
1 silicon	10 ± 3	3.4 ± 0.1	0 ± 3	2 ± 1	
2 water	7 ± 2		100	3 ± 1	
3 headgroup	6 ± 2	1.0 ± 0.3	7 ± 3	3 ± 2	
4 alkane	33 ± 1	0.7 ± 0.1	9 ± 4	4 ± 3	
5 headgroup	34 ± 5	1.9 ± 0.4	57 ± 3	17 ± 4	
6 protein	97 ± 5	3.6 ± 0.4	62 ± 5	15 ± 4	
7 protein	71 ± 6	4.5 ± 0.4	68 ± 5	16 ± 4	2.1

parameters. The results resemble the overall model parameters obtained from the analysis of the X-ray profile (Table 1). The fitted overall thickness of the two additional boxes for the glycoprotein layer is 277 ± 6 Å. This consists of two layers of thickness 115 ± 5 and 162 ± 6 Å, with respective SLDs of $3.6 \pm 0.4 \times 10^{-6}$ and $4.2 \pm 0.4 \times 10^{-6}$ $Å^{-2}$ and a roughness value of 12 ± 4 Å (Table 2). Figure 4c shows the calculated SLD profile. The box attributed to the lipid headgroup showed a significant change in the thickness and SLD (Table 2), and attempts to further distinguish the lipid headgroup from the PSA−NCAM did not improve the fit. The 5 Å increase in the "head group" box from 19 to 24 ± 6 Å is attributed to the reduced contrast between the glycoprotein and headgroup and is ascribed to the protein. The overall glycoprotein thickness is thus ∼284 Å, in good agreement with the 290 Å thickness obtained by XR. The reduced hydration in these two glycoprotein layers relative to that of the unmodified NCAM is consistent with the increased surface coverage of PSA−NCAM, measured by SPR (Figure 2). The increased thickness of the protein layers, along with the increase in the SLD of the glycoprotein box(es), also agrees with the X-ray model. These data support the hypothesis that the excluded volume of the PSA extends beyond the unmodified NCAM at near-physiological NaCl concentrations.

To investigate the effect of ionic strength on the excluded volume of the PSA, the buffer bathing the protein was exchanged with one containing 1 M NaCl. The comparison was with the same sample, so that the only change would be due to ionic-strength-dependent changes in the polymer configuration. Figure 4b shows the reflectivity profile of PSA−NCAM-His_{10} bathed in buffered D_2O containing 1 M NaCl. Again, the data were fit by describing the glycoprotein by two additional boxes, in addition to the layers for the lipid, oxide, and thin water film. Table 2 gives the results of the box-fitting algorithm. In contrast to the model obtained with 100 mM NaCl, the best model fit to the data in Figure 4b shows a clear reduction in the overall glycoprotein thickness to 168 Å (=97 + 71 Å). In addition, the hydration in both layers decreased significantly. In turn, this increased the overall SLD β_{meas} (eq 1) near the base of the protein. We attribute this reduction in the glycoprotein thickness, together with the "dehydration" of the layer, to a reduction in the carbohydrate extension and an increase in the segment density near the protein base. The "NTA-linker" box is also broader, because of the decreased contrast between the tethered NTA and the glycoprotein. The overall thicknesses of the glycoprotein monolayers determined from model fits to both the XR and NR data at this high salt concentration agree qualitatively with each other. Both also agree with the expected reduction in the excluded volume of the PSA because of electrostatic screening of the sialic acid charges at high ionic strength.

DISCUSSION

The properties of the NTA-TRIG-DLGE monolayer and supported bilayer determined in this study are in excellent agreement with prior results. The electron-density profile obtained from the analysis of the XR spectrum of the Ni-NTA-TRIG-DLGE monolayer is described by two distinct regions. The determined thickness and electron density of the alkane region match the previous reflectivity analysis of the Ni-NTA-TRIG-DLGE monolayer that reported an alkane layer thickness of 14.5 Å (*25*). The fitted thickness of the hydrophilic headgroup also agrees with the previous report, within the error of ±3 Å and ±0.01 $e^-/Å^{-3}$. This demonstrates the reproducibility of the monolayer assembly and lipid organization.

The analysis of the NR profile of the lipid bilayer under the constraints of two solvent contrasts and the use of physically realistic parameters yielded a model with values expected for an intact, homogeneous lipid bilayer. The superficial oxide layer of the silicon block is separated from the bilayer by a thin water film. The bilayer is composed of three layers, namely, a DPPC headgroup, an alkane layer, and the NTA-TRIG-DLGE headgroup. The fitted DPPC headgroup thickness is within 2 Å of that previously reported (*29*). The fitted alkane layer thickness of 32 ± 1 Å agrees with the measured values of 17.5 Å for the gel-phase hydrocarbon tails of DPPC (*31*) and the measured 13 ± 1 Å hydrocarbon thickness of the fluid NTA-TRIG-DLGE [Table 1 (*25*)]. From the neutron data, the thickness of the hydrated NTA-TRIG-DLGE headgroup was modeled as a single layer, with a slightly greater thickness than determined by XR. Overall, the models of the lipids obtained with both the neutron and X-ray data agree with the known values for these lipid layers.

The model parameters for the NCAM ectodomain obtained by both XR and NR support a model in which the membrane-bound NCAM ectodomain is bent. In both reflectivity models, the single box describing the full NCAM ectodomain was much smaller than the 280 Å end−end length expected if the seven domains adopted a rigid, linear structure oriented perpendicular to the membrane. This shorter-than-expected thickness also agrees qualitatively with the measured steric thickness of the protein monolayers determined by direct-force measurements (*17*). In contrast, force measurements showed that the Ig1−5 segment of NCAM is extended and orients normal to the membrane (*17*). The polyhistidine tag and NTA tether do not therefore tilt the protein. These data suggest that the bend in the ectodomains seen in the EM images is C-terminal to the fifth Ig domain (*5*, *6*). This hinge would tilt the protein relative to the surface normal and reduce the net protein extension (thickness) perpendicular to the membrane. A model interpretation of these data is shown in parts b and c of Figure 5.

The NR and XR results for NCAM are in close agreement. Close inspection of the unmodified NCAM thickness values obtained with the X-ray and neutron models shows a slight quantitative difference. This could be due to a combination of experimental error and the protein layer roughness or to the influence of the different underlying substrates.

The increase in the thickness of the PSA−NCAM-His_{10} relative to that of the NCAM-His_{10} suggests the mechanism by which PSA inhibits cell adhesion. Parts b and c of Figure 5 show the structural interpretations of the XR and NR models of PSA−NCAM-His_{10} monolayers in 100 mM and 1 M NaCl solutions, respectively. In both the XR and NR data, the best-fit models of the overall thickness of the PSA−NCAM layer in 100 mM NaCl agree within 5 Å, and the roughness values for the glycoprotein layers are high in both cases. The glycoprotein thickness from both independent models shows a large increase in the overall thickness relative to that of the unmodified NCAM. These data show quanti-

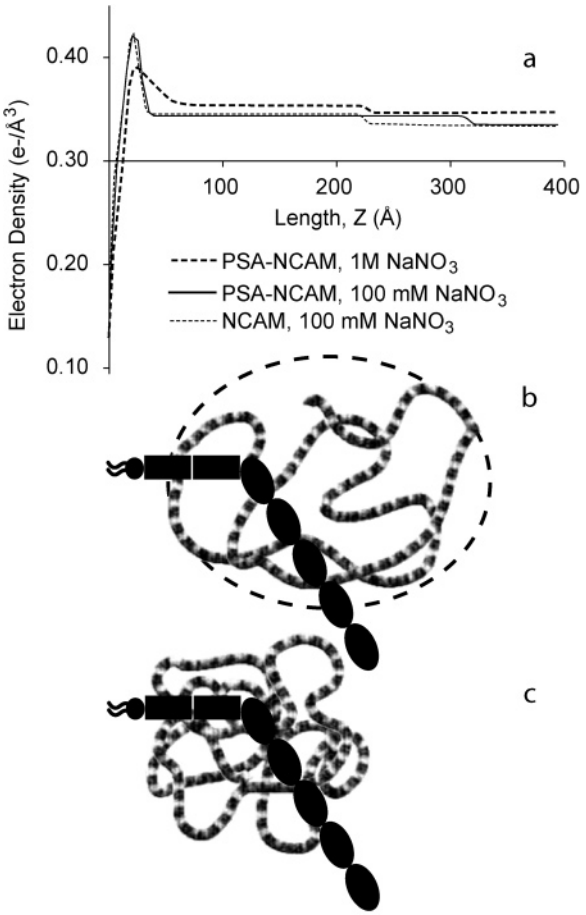

FIGURE 5: Model interpretations of the electron-density profiles in Figures 3c and 4c. The box models describing the XR profiles are shown in a. The black figure in b and c indicates the NCAM ectodomain configuration compatible with the measured thickness and proposed bend in the structure. The structure in b shows the proposed excluded volume of the PSA in 100 mM NaCl, and the structure in c indicates the excluded volume of PSA in 1 M NaCl.

tatively that the PSA chains extend beyond the protein core at near-physiological NaCl. These findings do not rule out additional effects of PSA on possible cis (lateral) interactions. However, the polymer dimensions would generate an electrosteric repulsive barrier that would prevent the close approach of opposed cells. This is further supported by recent force measurements between PSA−NCAM monolayers, which show that NCAM sialylation increases the range and magnitude of the interbilayer repulsion and abrogates NCAM-mediated adhesion (*35*).

The extension L of grafted polyelectrolyte chains normal to a surface depends on the molecular weight and grafting density (*14*). It is possible that the chains are stretched because of crowding at the NCAM densities used in this work. On the basis of antibody-labeling studies, the NCAM density on F11 cells is ~98 μm^{-2}, which is about 40 times lower than used in these measurements. On the other hand, a different study showed that NCAM is located in clusters (*32*), which would have a higher local density. It is difficult to say which of these is the most physiologically relevant. It is useful to consider the range of possible polymer extensions over a range of NCAM densities. At a 40-fold lower density where there is little lateral-chain interactions, the polymer will adopt the configuration of free chains in solution. In solution, sialylation doubled the hydrodynamic radius of NCAM (*27*), indicating that the excluded volume of the chains is larger than the protein core. For charged polymers in good solvent and monovalent electrolyte, the theoretically predicted size of the PSA ($N = 100$) would be ~76 nm (*33*). The size also scales with $N^{3/5}$ (*33*). Because the chains are grafted to Ig domain 5, which is 90 nm from the membrane surface, ideal, freely jointed, monodisperse chains would extend $90 + 76 = 166$ nm from the membrane. Under these conditions, they would still envelop 83% of the ectodomain and interfere sterically with binding between fully overlapping Ig1−5 segments and antiparallel Ig12 domains (*17*).

These measurements provide a structural interpretation of the ionic strength dependence of adhesion between cells expressing PSA−NCAM (Figure 5). The fitted model for PSA−NCAM in 1 M NaCl (parts a and c of Figure 5) shows a significant shift in both the electron density and the SLD. In the XR and NR models, the overall thickness decreases and the segment density near the base of the protein increases. These results confirm previous evidence for the reduction in the excluded volume of PSA at high ionic strength (*27*). They show further that, in 1 M NaCl, the PSA does not extend beyond the range of the NCAM ectodomain, because the SLD of the outer layer in the neutron studies matches that of the unmodified NCAM. The polymer-segment density clearly shifts at high ionic strength, such that the N-terminal Ig domains could lie outside the excluded volume occupied by the carbohydrate. These results can explain the recovery of adhesion between PSA−NCAM-expressing cells in 0.5 M NaCl (*27*). The chain collapse reported in this study would reduce the range and magnitude of the osmotic repulsion between cells and possibly expose the outer Ig domains. Both effects would increase the adhesion between adjacent cells.

For the PSA−NCAM models in both 100 mM and 1 M NaCl, the glycoprotein/subphase interface was rough. This degree of interfacial roughness is most likely due to the polydispersity of the carbohydrate, which would generate a gradual decay in the density profile rather than the sharp cutoff assumed in the box model. This dispersity could also affect the configuration of the collapsed brush at high ionic strength, if most of the PSA occupies the reduced volume but some chains extend beyond the collapsed configurations. Indeed, a recently published theoretical description of a bidisperse anisotropic brush predicted that the segment-density profile would decrease gradually (*34*). However, given the limited contrast in these measurements, we are unable to elaborate on more subtle features of the carbohydrate-density profile.

In summary, these structural analyses support the hypothesis that PSA regulates NCAM function and cell adhesion in general, by increasing the excluded volume of glycoprotein and the associated range and magnitude of the repulsive pressure between adjacent cells. Despite the independent fitting of both the NR and XR data, the resultant models agree qualitatively for every sample in which a comparison can be made. It is also important to point out that, even though all parameters were allowed to vary in the fitting procedures, they are constrained by physically realistic models of these well-characterized systems (*17*, *25*, *29*). For example, the thicknesses, electron densities, and SLDs of

the lipid layers agree with previously determined values (*25*, *29*). Moreover, from fits of spectra obtained with adsorbed NCAM, the parameters for the lipids agreed with values determined both in prior reports and in measurements of the identical layers prior to the protein adsorption. Furthermore, the fitted thickness of the protein agreed with the steric thickness quantified in direct-force measurements (*17*). The added constraints placed on the global fits of the NR data and the use of multiple contrasts further eliminated many models that would be considered degenerate with only one solvent contrast. It should be noted that the fits are to the models and do not constitute direct evidence of the structure of the glycoprotein. Nevertheless, the agreement between the parameters thus determined and these several physical constraints, together with the consistency of the independent XR and NR analyses, results in a high degree of confidence for the conclusions reached.

ACKNOWLEDGMENT

We acknowledge the ESRF for provision of beam time and facilities, and we thank Leide Cavalcanti for assistance. We also acknowledge the Institute Laue Langevin for provision of neutron beam time and facilities, and we thank Robert Cubitt and Barry Stidder for assistance. We also thank Nancy Harmon for her technical assistance with the protein production.

REFERENCES

1. Doherty, P., Walsh, F. S. (1996) CAM−FGF receptor interactions: A model for axonal growth, *Mol. Cell. Neurosci. 8*, 99−111.
2. Doyle, E., Nolan, P. M., Bell, R., Regan, C. M. (1992) Intraventricular infusions of anti-neural cell adhesion molecules in a discrete posttraining period impair consolidation of a passive avoidance response in the rat, *J. Neurochem. 59*, 1570−1573.
3. Cunningham, B. A., Hemperly, J. J., Murray, B. A., Prediger, E. A., Brackenbury, R., Edelman, G. M. (1987) Neural cell adhesion molecule: Structure, immunoglobulin-like domains, cell surface modulation, and alternative RNA splicing, *Science 236*, 799−806.
4. He, H. T., Barbet, J., Chaix, J. C, Goridis, C. (1986) Phosphatidylinositol is involved in the membrane attachment of NCAM-120, the smallest component of the neural cell adhesion molecule, *EMBO J. 5*, 2489−2494.
5. Hall, A., Rutishauser, U. (1987) Visualization of neural cell adhesion molecule by electron microscopy, *J. Cell Biol. 104*, 1579−1586.
6. Becker, J. W., Erickson, H. P., Hoffmann, S., Cunningham, B. A., Edelman, G. M. (1989) Topology of cell adhesion molecules, *Proc. Natl. Acad. Sci. U.S.A. 86*, 1088−1092.
7. Nelson, R. W., Bates, P. A., Rutishauser, U. (1995) Protein determinants for specific polysialylation of the neural cell adhesion molecule, *J. Biol. Chem. 270*, 17171−17179.
8. Walsh, F., Doherty, P. (1997) Neural cell adhesion molecules of the immunoglobulin superfamily, *Annu. Rev. Cell. Biol. 13*, 425−456.
9. Bruses, J., Rutishauser, U. (2001) Roles, regulation, and mechanism of polysialic acid function during neural development, *Biochimie 83*, 635−643.
10. Tang, J., Landmesser, L., Rutishauser, U. (1992) Polysialic acid influences specific pathfinding by avian motoneurons, *Neuron 8*, 1031−1044.
11. Rutishauser, U. (1992) NCAM and its polysialic acid moiety: A mechanism for pull/push regulation of cell interactions during development? *Development Suppl.*, 99−105.
12. Rutishauser, U. (1996) Polysialic acid and the regulation of cell interactions, *Curr. Opin. Cell Biol. 8*, 679−684.
13. Livingston, B., Jacobs, J. L., Glick, M. C., Troy, F. A. (1988) Extended polysialic acid chains (*n* greater than 55) in glycoproteins from human neuroblastoma cells, *J. Biol. Chem. 263*, 9443−9448.
14. Pincus, P. (1991) Colloid stabilization with grafted polyelectrolytes, *Macromolecules 24*, 2912−2919.
15. Yang, P., Yin, X., Rutishauser, U. (1992) Intercellular space is affected by polysialic acid content of NCAM, *J. Cell Biol. 116*, 1487−1496.
16. Fujimoto, I. B. J.; Rutishauser U. (2001) Regulation of cell adhesion by polysialic acid. Effects on cadherin, immunoglobulin cell adhesion molecule, and integrin function and independence from neural cell adhesion molecule binding or signaling activity, *J. Biol. Chem. 276*, 31745−31751.
17. Johnson, C. P., Fujimoto, I., Perrin-Tricaud, C., Rutishauser, U., Leckband, D. (2004) Mechanism of homophilic NCAM adhesion: Use of multiple domains and flexibility, *Proc. Natl. Acad. Sci. U.S.A. 101*, 6963−6968.
18. Konovalov, O., Myagkov, I., Struth, B., Lohner, K. (2002) Lipid discrimination in phospholipid monolayers by the anti-microbial frog skin peptide PGLa. A synchrotron X-ray grazing incidence and reflectivity study, *Eur. Biophys. J. 31*, 428−437.
19. Konovalov, O., Struth, B., Smilgies, D. M. (2003) Troika II (ID10B): A versatile beamline for studies of liquid and solid interfaces, *AIP Conf. Proc. SRI-2003*, 2.
20. Cubitt, R., Fragneto, G. (2002) D17: The new reflectometer at the ILL, *Appl. Phys. A: Matter. Sci. Process. 74*, S329−S331.
21. Charitat, R., Bellet-amalric, E., Fragnetto, G., Graner, F. (1999) Adsorbed and free lipid bilayers at the solid−liquid interface, *Eur. Phys. J. B 8*, 583−593.
22. Lavrik, N., Leckband, D. (2000) Optical and direct force measurements of the interaction between monolayers of aromatic macrocycles on surfactant monolayers, *Langmuir 16*, 1842−1851.
23. Yeung, C., Purves, T., Kloss, A. A., Kuhl, T. L., Sligar, S., Leckband, D. (1999) Cytochrome *c* recognition of immobilized, orientational variants of cytochrome *b*5: Direct force and equilibrium binding measurements, *Langmuir 15*, 6829−6836.
24. Vaknin, D., Als-Nielsen, J., Piepenstock, M., Lösche, M. (1991) Recognition processes at a functionalized lipid surface observed with molecular recognition., *Biophys. J. 60*, 1545−1552.
25. Martel, L., Johnson, C., Boutet, S., al-Kurdi, R., Konavalov, O., Robinson, I., Leckband, D., and Legrand, J.-F. (2002) X-ray reflectivity investigations of two-dimensional assemblies of C-cadherins: First steps in structural and functional studies, *J. Phys. IV France 12*, 365−377.
26. Weygand, M., Schalke, M., Howes, P. B., Kjaer, K., Friedmann, J., Wetzer, B., Pum, D., Sleytr, U. B., Lösche, M. (1999) Coupling of protein sheet crystals (S-layers) to phospholipid monolayers, *J. Mater. Chem. 10*, 141−148.
27. Yang, P., Major, D., Rutishauser, U. (1994) Role of charge and hydration in effects of polysialic acid on molecular interactions on and between cell membranes, *J. Biol. Chem. 269*, 23039−23044.
28. Thirtle, P. N. (1996) *AFIT: Coupled Simulation Program*, see http://www.ill.fr/Computing.
29. Fragneto, G., Graner, F., Charitat, T., Dubos, P., Bellet-Amalric, E. (2000) Interaction of the third helix of antennapedia homeodomain with a deposited phospholipid bilayer: A neutron reflectivity structural study, *Langmuir 16*, 4581−4588.
30. Kuhl, T. L., Majewski, J., Wong, J. Y., Steinberg, S., Leckband, D. E., Israelachvili, J. N., Smith, G. S. (1998) A neutron reflectivity study of the polymer-modified phospholipid monolayers at the solid-solution interface: Polyetheylene glycol-lipids on silane-modified substrates, *Biophys. J. 75*, 2352−2362.
31. Vierl, U., Cevc, G. (1997) Time-resolved X-ray reflectivity measurements of protein binding onto model lipid membranes at the air−water interface, *Biochem. Biophys. Acta 1325*, 165−177.
32. Rusakov, D. A., Davies, H. A., Stewart, M. G., Schachner, M. (1995) Clustering and co-localization of immunogold double labelled neural cell adhesion molecule isoforms in chick forebrain, *Neurosci. Lett. 93*, 170−175.
33. Schiessel, H. (1999) Counterion condensation on flexible polyelectrolytes: Dependence on ionic strength and chain concentration, *Macromolecules 32*, 5673−5680.
34. Amoskov, V., Birshtein, T. M. (2001) Polydisperse anisotropic brushes, *Macromolecules 34*, 5331−5341.
35. Johnson, C. P., Fujimoto, I., Rutishauser, U., Leckband, D. E. (2005) Direct evidence that NCAM polysialylation increases intermembrane repulsion and abrogates adhesion, *J. Biol. Chem.*, in press.

BI048263J